

# *Why does Arakawa and Schubert's convective quasi-equilibrium closure not work? Mathematical analysis and implications*

Article

Accepted Version

Yano, J.-I. and Plant, B. ORCID: <https://orcid.org/0000-0001-8808-0022> (2020) Why does Arakawa and Schubert's convective quasi-equilibrium closure not work? Mathematical analysis and implications. *Journal of the Atmospheric Sciences*, 77 (4). pp. 1371-1385. ISSN 1520-0469 doi: <https://doi.org/10.1175/jas-d-19-0165.1> Available at <https://centaur.reading.ac.uk/87845/>

It is advisable to refer to the publisher's version if you intend to cite from the work. See [Guidance on citing](#).

To link to this article DOI: <http://dx.doi.org/10.1175/jas-d-19-0165.1>

Publisher: American Meteorological Society

All outputs in CentAUR are protected by Intellectual Property Rights law, including copyright law. Copyright and IPR is retained by the creators or other copyright holders. Terms and conditions for use of this material are defined in the [End User Agreement](#).

[www.reading.ac.uk/centaur](http://www.reading.ac.uk/centaur)

**CentAUR**

Central Archive at the University of Reading

Reading's research outputs online

1 **Why Does**  
2 **Arakawa and Schubert's Convective Quasi-Equilibrium Closure**  
3 **Not Work?**  
4 **Mathematical Analysis and Implications**

5 Jun-Ichi Yano\*

6 *CNRM, Météo-France and CNRS, UMR 3589, 31057 Toulouse Cedex, France*

7 Robert S. Plant

8 *Department of Meteorology, University of Reading, UK.*

9 \*Corresponding author address: CNRM, Météo-France, 42 av Coriolis, 31057 Toulouse Cedex,  
10 France.

11 E-mail: [jiy.gfder@gmail.com](mailto:jiy.gfder@gmail.com)

## ABSTRACT

12 Arakawa and Schubert (1974) proposed convective quasi-equilibrium as a  
13 guiding principle for the closure of convection parameterization. However,  
14 empirical experiences from operational implementation efforts suggest that  
15 its strict application does not work well. The purpose of the present paper  
16 is to explain mathematically why this closure does not work in practice, and  
17 to suggest that problems stem from physically unrealistic assumptions. For  
18 this purpose, the closure hypothesis is examined in its original form, and  
19 without imposing a condition of a positiveness to the convective mass fluxes.  
20 The Jordan sounding with idealized large-scale forcing is used for diagno-  
21 sis purposes. The question is addressed from several perspectives including  
22 the completeness of the entraining plume spectrum, and a singular vector de-  
23 composition of the interaction kernel matrix. The main problems with the  
24 quasi-equilibrium closure are traced to: (i) the relatively slow response of  
25 shallower convective modes to large-scale forcing; and, (ii) detrainment at  
26 convection top producing strong cooling and moistening. A strict application  
27 of the convective quasi-equilibrium principle leads to a singular response of  
28 shallow convection. An explicit coupling of convection with stratiform clouds  
29 would be crucial for preventing this unrealistic behavior, recognizing that the  
30 re-evaporation of detrained cloudy-air is a relatively slow process.

32 **1. Introduction**

33 Closure is a key issue in the convection parameterization problem (*cf.*, Yano *et al.* 2013). Con-  
 34 vective quasi-equilibrium, as originally proposed by Arakawa and Schubert (1974: see Yano and  
 35 Plant 2012a as a review), remains an important guiding principle for the convective closure even  
 36 today (*e.g.*, Zhang 2002, 2003, Donner and Phillips 2003, Bechtold *et al.* 2014), in spite of various  
 37 criticisms (*e.g.*, Houze and Betts 1981, Mapes 1997).

38 The quasi-equilibrium closure may be formally stated for a spectral form of mass-flux convec-  
 39 tion parameterization as:

$$40 \quad \mathbf{K}\vec{\mathbf{M}} + \vec{\mathbf{F}} = 0. \quad (1.1)$$

41 Here,  $\mathbf{K}$  is an interaction matrix (kernel in Arakawa and Schubert, 1974) that describes the feed-  
 42 back from the mass-flux vector (spectrum),  $\vec{\mathbf{M}}$ , onto the large-scale tendency of an instability  
 43 measure known as the cloud work function;  $\vec{\mathbf{F}}$  is the spectrum of large-scale forcing for the cloud  
 44 work function, which is also defined as a vector. The vector components correspond to convective  
 45 plume types that represent a spectrum of convective towers. The cloud work function corresponds  
 46 to the rate at which available potential energy is converted into convective kinetic energy, as nor-  
 47 malized by the mass flux at the convection base (*cf.*, Yano *et al.* 2005a). Here, the equilibrium  
 48 assumption states that the total tendency vanishes. Generalizations of the quasi-equilibrium ideas  
 49 are discussed by Yano and Plant (2016).

50 Eq. (1.1) states that the convective response (1st term) is always in balance with the large-scale  
 51 forcing (2nd term). This closure is, intuitively speaking, physically sound, because the convective  
 52 process is much faster than the large-scale processes. However, in spite of a series of subsequent  
 53 efforts, this original form of the closure has never become fully operational, but only in variant

54 forms (*e.g.*, Moorthi and Suarez 1992). This study will explain why the formulation given by  
55 Eq. (1.1) is structurally difficult to implement as a closure from a mathematical point of view.

56 The original implementation (Lord and Arakawa 1980, Lord 1982, Lord *et al.* 1982) devoted  
57 much attention to maintaining positiveness of the convective mass fluxes, because only convective  
58 updrafts were considered. Unfortunately, in our opinion and as we will discuss below, a rather  
59 elaborate iteration procedure introduced for this purpose may have obscured some more basic  
60 issues with a strict convective quasi–equilibrium closure.

61 The present study focuses on the closure problem exactly as given by Eq. (1.1) without any  
62 further restrictions. This strategy may be partially justified by considering negative mass–fluxes  
63 as detraining downdrafts (*i.e.*, time–reversed updrafts). Importantly, regardless of whether this  
64 reinterpretation stands or not, this simplification enables us to elucidate more clearly and cleanly  
65 some basic problems with Arakawa and Schubert’s (1974) original convective quasi–equilibrium  
66 closure.

67 For the same reason, the original assumption of a spectrum of purely entraining plumes is main-  
68 tained in the present study, because we believe it is important to establish a baseline. In the lit-  
69 erature, the problems with the oversimplified entraining–plume hypothesis have been extensively  
70 discussed, and various alternative formulations have been proposed, as reviewed in *e.g.*, de Rooy  
71 *et al.* (2013), Yano (2014a). Analysis with a more elaborate plume model would be considered a  
72 future work.

73 A simple formulation for the terms in Eq. (1.1) is provided in the next section, and some basic  
74 demonstrations of the problems are made in Sec. 3. The identified problems are investigated in  
75 Sec. 4 by examining the completeness of the entraining-plume spectrum as well as the mathemat-  
76 ical structure of the interaction (kernel) matrix.

77 The present paper focuses on a rather narrow question of mathematical difficulties with the orig-  
78 inal closure formulation by Arakawa and Schubert (1974). Various physical issues associated with  
79 this closure hypothesis as well as with the mass–flux formulation itself are extensively discussed  
80 in the literature. Some of these may be found in a review of uasi-equilibrium by Yano and Plant  
81 (2012), and more general issues associated with the mass–flux parameterization are covered by  
82 Plant and Yano (2015). In concluding, in Sec. 5, the paper also turns to the physical implications  
83 from the present findings, also referring to background issues.

## 84 **2. Formulation**

### 85 *a. Data*

86 A tropical climatology based on the Jordan sounding (Jordan 1958) is adopted for specifying  
87 vertical profiles of temperature and moisture. The vertical resolution used for the profile data is  
88 50 hPa from 1000 to 200 hPa, and with a surface value at 1015 hPa being separately given. Data  
89 is also available further above at 175, 150, 125, 100, 80, 60, 50, 40, and 30 hPa levels.

90 We introduce idealized large–scale advective forcings defined by

$$91 \quad F_L[T] = -\bar{w} \left( \frac{\bar{T}}{\bar{\theta}} \right) \frac{d\bar{\theta}}{dz} \quad (2.1a)$$

$$92 \quad F_L[q_v] = -\bar{w} \frac{d\bar{q}_v}{dz} \quad (2.1b)$$

94 for temperature and moisture, respectively. Here,  $\bar{T}$ ,  $\bar{\theta}$ ,  $\bar{q}_v$  are the vertical profiles for the tem-  
95 perature, the potential temperature, and the moisture as provided by the Jordan sounding. The  
96 large–scale vertical velocity,  $\bar{w}$ , in Eq. (2.1) is prescribed by

$$97 \quad \bar{w}(z) = \begin{cases} w_0 \sin \pi \left[ \frac{p(z) - p(z_T)}{p_0 - p(z_T)} \right] & \text{for } p_0 \geq p(z) \geq p(z_T) \\ 0 & \text{for } p(z_T) > p(z) \end{cases} \quad (2.2)$$

98 as a function of the pressure,  $p(z)$ , with  $w_0 = 10^{-2} \text{ ms}^{-1}$ , and  $p_0 = 1015 \text{ hPa}$  the surface pressure.

99 Three types of large–scale forcing are considered: deep ( $z_T = 15 \text{ km}$ ), shallow ( $z_T = 5 \text{ km}$ ), and

100 very shallow ( $z_T = 1.5$  km). The purpose of this idealization is to examine the convective response  
101 to large-scale forcing strictly confined to a certain vertical range. These forcing profiles are shown  
102 in Fig. 1(a). Here, as a drastic simplification, potential contributions to the forcing from boundary-  
103 layer processes are neglected, despite their possible importance. Consistent with that assumption,  
104 contributions from boundary-layer processes to the interaction matrix,  $\mathbf{K}$ , will also be neglected  
105 in the analysis below.

106 The large-scale forcing on the cloud work function,  $\vec{\mathbf{F}}$  from Eq. (1.1), is obtained by vertically  
107 integrating a linear combination of two large-scale forcings, as explicitly given by Eq. (B33) in  
108 Arakawa and Schubert (1974). The integration is defined with a weighting that is a function  
109 of the fractional entrainment rate,  $\varepsilon$  (see next subsection), and the resulting integrated forcing  
110 is presented in Fig. 1(b). We remark that the forcing has a relatively weak dependence on a  
111 microphysical parameter,  $c_0$ , which is defined by Eq. (2.5) below in Sec. 2.c. The vertical profile  
112 of the large-scale forcing as defined by Eqs. (2.1a,b) and (2.2) has a well-defined vertical scale  
113 but its projection onto the plume components in Fig. 1(b), presents a very broad distribution of  
114 forcing as a function of the entrainment rate, despite the fact that the entrainment rate determines  
115 the vertical scale of each plume mode. Moreover, the main difference from changing the vertical  
116 scale of large-scale forcing is a change of the spectrum amplitude rather than a change of the  
117 spectrum shape.

118 We diagnose the convective quasi-equilibrium closure of Eq. (1.1) by closely following the  
119 mass-flux spectrum formulation introduced by Arakawa and Schubert (1974), and for formula-  
120 tion details we refer to the original paper. In the following two subsections, we describe two major  
121 assumptions for which some additional specifications are required: the entraining-plume spectrum  
122 (Sec. 2.b) and the precipitation formulation (Sec. 2.c).

### 123 *b. Entraining-Plume Spectrum*



124 Arakawa and Schubert's (1974) entraining-plume spectrum is characterized by a set of constant  
 125 fractional entrainment rates,  $\varepsilon_i$ , which are defined in this study by:

$$126 \quad \varepsilon_i = \frac{i - 1/2}{n} \varepsilon_{\max}, \quad (2.3)$$

127 where the vector index,  $i$ , spans for  $i = 1, \dots, n$  with  $n = 20$  plume types considered, and  $\varepsilon_{\max} =$   
 128  $10^{-4} \text{ m}^{-1}$  is the maximum fractional entrainment rate considered. The  $i$ -th entraining plume has  
 129 a normalized mass-flux profile of

$$130 \quad \eta_i(z) = \begin{cases} \exp[-\varepsilon_i(z - z_B)] & \text{for } z_B \leq z \leq z_{Ti} \\ 0 & \text{otherwise} \end{cases} \quad (2.4)$$

131 where  $z_B$  and  $z_{Ti}$  are the bottom and top levels of the plume. The base level,  $z_B$ , is taken to be  
 132 950 hPa (583 m), approximately corresponding to the top of the convectively well-mixed boundary  
 133 layer. The top,  $z_{Ti}$ , is defined by the level of neutral buoyancy, at which all of the plume air  
 134 detrain into the environment. The top height,  $z_{Ti}$ , is diagnosed as a continuous function by taking  
 135 a linear interpolation of values between the data height levels and we assume that the plume-top  
 136 detrainment happens over a vertical layer spanning between these two levels.

137 For a larger fractional entrainment rate,  $\varepsilon$ , the in-plume air is more diluted by the environmental  
 138 air, and so becomes less buoyant. As a result, the plume top height,  $z_{Ti}$ , decreases with increasing  
 139  $\varepsilon$ . In essence, the fractional entrainment rate,  $\varepsilon$ , becomes a reverse measure of the convection  
 140 depth,  $z_T$ . Some examples of vertical profiles of entraining plumes for the Jordan sounding are  
 141 shown in Fig. 2. A full mass-flux profile for the  $i$ -th plume is defined by  $M_i \eta_i(z)$ , where  $M_i$  is the  
 142 mass flux at the plume base for the plume type and is the  $i$ -th component of the mass-flux vector  
 143  $\vec{M}$  in Eq. (1.1).

144 *c. Precipitation efficiency*

145 A very simple cloud microphysics is used, in which the precipitation rate,  $R_i$ , within the  $i$ -th  
 146 plume at each vertical level is assumed to be proportional to the cloud–water vertical flux,  $w_{ci}q_{ci}$ ,  
 147 with a proportionality constant,  $c_0$ , called the precipitation efficiency:

$$148 \quad R_i = c_0 w_{ci} q_{ci}.$$

149 Here,  $w_{ci} = M_i \eta_i / \rho \sigma_i$  and  $q_{ci}$  are respectively the in-cloud vertical velocity and the cloud–water  
 150 mixing ratio of the  $i$ -th plume type, and  $\rho$  is the air density. The precipitation rate,  $R_i$ , is defined  
 151 in such a manner that the fractional area,  $\sigma_i$ , occupied by the  $i$ -th plume type does not appear in  
 152 actual calculations of the total–water for a given plume type (*cf.*, Eq. 6.2b of Yano 2015).

153 The precipitation efficiency,  $c_0$ , is chosen by following a curve shown in Hack *et al.* (1984: their  
 154 Fig. 3). Specifically, we take

$$155 \quad c_0 = -\frac{2\Delta c}{\pi} \arctan\left(\frac{\varepsilon - \varepsilon_0}{\varepsilon_c}\right) + c_{00}, \quad (2.5)$$

156 where  $c_{00} = (c_{\max} + c_{\min})/2$  and  $\Delta c = (c_{\max} - c_{\min})/2$ . Note that  $c_0 \rightarrow c_{\max}$  and  $c_0 \rightarrow c_{\min}$  as  
 157  $\varepsilon \rightarrow 0$  and  $\varepsilon \rightarrow \infty$ , respectively;  $\varepsilon_0$  marks a transition from a weakly–precipitating shallow (with  
 158 large  $\varepsilon$ ) to a heavily–precipitating deep (with small  $\varepsilon$ ) regime. Here, the parameters are set as  
 159  $\varepsilon_0 = 5 \times 10^{-5} \text{ m}^{-1}$ ,  $c_{\max} = 4.5 \times 10^{-3} \text{ m}^{-1}$ ,  $c_{\min} = 5 \times 10^{-5} \text{ m}^{-1}$ , and  $\varepsilon_c = 10^{-6} \text{ m}^{-1}$ . Figure 3  
 160 plots the precipitation efficiency,  $c_0$ , as a function of the fractional entrainment rate,  $\varepsilon$ .

### 161 **3. Basic Analyses**

#### 162 *a. Interaction matrix*

163 The interaction matrix (kernel),  $\mathbf{K}$ , is defined by Eq. (B32) and Eqs. (B35)–(B38) of Arakawa  
 164 and Schubert (1974). Its evaluation using Eq. (2.5) for the precipitation efficiency is shown  
 165 in Fig. 4(a). An element,  $K_{ij}$ , of the interaction matrix defines the rate at which a unit of the  
 166 convection-base mass flux for the  $j$ -th plume type,  $M_j$ , changes the cloud-work function for the  
 167  $i$ -th plume type.

168 By referring to Eq. (144) and Fig. 11 of Arakawa and Schubert (1974), we find that the large–  
 169 scale thermodynamic profiles are modified by convection in two major ways: (i) detrainment at  
 170 the plume top, which cools and moistens the large–scale environment due to evaporation of the  
 171 detrained cloudy air; and, (ii) a compensating descent in the large–scale environment, which leads  
 172 to adiabatic heating and drying by downward transport of drier air from aloft. These two major  
 173 processes modify the cloud–work function, and the interaction matrix can be separated into two  
 174 dominant contributions:

$$175 \quad \mathbf{K} = \mathbf{K}_d + \mathbf{K}_v, \quad (3.1)$$

176 where  $\mathbf{K}_d$  and  $\mathbf{K}_v$  represent the effects of detrainment and environmental descent, respectively. A  
 177 third part,  $\mathbf{K}_M$ , as defined by Eq. (B32) of Arakawa and Schubert (1974), is neglected because of  
 178 our assumptions above about boundary layer processes.

179 The evaporative cooling associated with detrainment leads to a further destabilization of the  
 180 atmosphere, and thus  $\mathbf{K}_d$  is positive definite (Fig. 4(b)). This tendency is stronger when a plume  
 181 is less–strongly precipitating, and hence for the shallower plumes with larger  $\varepsilon'$ . Moreover, the  
 182 detrainment effect is felt only by the plume types that extend higher than the detrainment level of  
 183 the plume in question (*i.e.*,  $\varepsilon < \varepsilon'$ ), and so  $\mathbf{K}_d$  is triangular. On the other hand, adiabatic heating  
 184 by environmental descent leads to a stabilization, and thus  $\mathbf{K}_v$  is negative definite (Fig. 4(c)). The  
 185 descent effect is stronger for deeper plumes with smaller  $\varepsilon'$ , and affects plume types of all depths.

### 186 *b. Response due to a single plume*

187 Once a value of  $M_i$ , as a component of the mass-flux vector,  $\vec{\mathbf{M}}$ , is specified [see also Eq. (3.2)  
 188 below], the tendencies of temperature and moisture produced by each convective plume type,  
 189  $i$ , can be calculated respectively from Eqs. (3.6a) and (3.6b) of Yano (2015). Examples of the  
 190 convective response from individual plume types are shown in Fig. 5. Here, we rather arbitrary  
 191 assume  $M_i = 10^{-2} \text{ kg m}^{-2} \text{ s}^{-1}$ . For the cases of  $\varepsilon = 6 \times 10^{-5}$  and  $8 \times 10^{-5} \text{ m}^{-1}$ , the resulting

192 plumes are relatively shallow, with relatively weak precipitation. This leads to strong cooling and  
 193 moistening at the detrainment level associated with cloud evaporation. The effects are much less  
 194 pronounced for the deep-plume example, because a high precipitation does not leave much cloud-  
 195 water for detrainment at the plume top. The values obtained for the strong cooling and moistening  
 196 associated with the detrained-air re-evaporation are shown in the Appendix to be consistent with  
 197 a simple scale analysis.

198 The strongly-peaked character of the thermodynamic tendencies from individual plume types  
 199 raises potential issues for construction of the total convective response, obtained by taking a linear  
 200 sum of these individual tendencies weighted by the convection-base mass-flux values,  $M_i$ . The  
 201 total response is considered next.

202 *c. Total Convective response*

203 The convective-base mass-flux vector,  $\vec{M} = (M_i)$ , is obtained from Eq. (1.1) by multiplying the  
 204 inverted matrix,  $\mathbf{K}^{-1}$ , on the large-scale forcing,  $\vec{F}$ . The obtained  $\vec{M}$ , shown in Fig. 6(a) as a  
 205 function of the fractional entrainment rate,  $\varepsilon$ , is marked by relatively large contributions from both  
 206 small and large  $\varepsilon$  with modest contributions from intermediate values. This basic structure is not  
 207 dependent on the depth of the large-scale forcing.

208 The resulting vertical profile of the total mass flux,  $M(z)$ , is given by

$$209 \quad M(z) = \sum_{i=1}^n \eta_i(z) M_i \quad (3.2)$$

210 and is shown in Fig. 6(b), where  $\eta_i(z)$  is the vertical profile of the  $i$ -th plume type, as defined by  
 211 Eq. (2.4).

212 The most noticeable feature is a strong downdraft below the 4-km level, which is the lowest  
 213 height achieved by plumes with largest fractional entrainment rates,  $\varepsilon$ , under the given mean ther-  
 214 mal profile. Above this level, a substantial updraft reaches the 14-km level under deep large-scale

215 forcing (solid curve), consistent with the depth of forcing in Fig. 1(a). It is replaced by an updraft  
 216 that decreases linearly with height between 4 and 14-km under shallow large-scale forcing (long  
 217 dash). This response is rather unintuitive considering the fact that shallow large-scale forcing only  
 218 reaches the 5-km level (*cf.*, Fig. 1). Only when very shallow large-scale forcing is considered  
 219 does the convective response above the 4-km level becomes negligible (short dash).

220 Figure 7 shows the corresponding convective tendency profiles for temperature (a) and moisture  
 221 (b). Clearly these do not match well with the forcings in Fig. 1, even though the cloud work  
 222 functions for each mode are in equilibrium by construction (*cf.*, Sec. 5.a). The sudden increase  
 223 of mass flux at the 4-km level (Fig. 6(b)) is associated with unrealistically strong heating and  
 224 drying, with magnitudes *c.a.*, 60 Kday<sup>-1</sup> for temperature and -120 Kday<sup>-1</sup> for moisture. The  
 225 peaks are manifestations of those seen for individual plume types in Fig. 5, but with the signs  
 226 reversed: entrainment (*i.e.*, negative cloud-top detrainment) at the top of detraining-downdraft  
 227 plumes causes this tendency. On the other hand, tendencies with more reasonable magnitudes are  
 228 found at the other vertical levels.

## 229 4. Further Analyses

### 230 a. Completeness of the spectrum of plumes

231 The basic idea of the spectrum model is to be able to represent every possible convective profile  
 232 using a sum of profiles from the individual plumes. Thus, we now ask whether the ensemble of  
 233 entraining plumes has such a capacity? The question may be more formally posed as the possibility  
 234 of decomposing any given arbitrary mass-flux profile,  $M(z)$ , by a plume spectrum given by the set  
 235 of functions  $\{\eta_i\}$  ( $i = 1, \dots, n$ ) as:

$$236 \quad M(z) = \sum_{i=1}^n \tilde{m}_i \eta_i(z), \quad (4.1)$$

237 where  $\tilde{m}_i$  are the expansion coefficients. Unfortunately, performing such a decomposition is not  
 238 straightforward, because the exponential entraining plume profiles of Eq. (2.4) do not constitute

239 an orthogonal set. Nevertheless, it is instructive to consider the issues further by assessing decom-  
 240 positions of both  $\eta_i$  and  $M$  using a complete orthonormal set. For this purpose, it is convenient to  
 241 use the vertical normal modes,  $W_i(z)$ , for the vertical velocity defined for the hydrostatic primitive  
 242 equation system (Kasahara and Puri 1981, Fulton and Schubert 1985). Thus, we set:

$$243 \quad \eta_j = \sum_{i=1}^n \hat{\eta}_{ij} W_i(z) \quad (4.2a)$$

$$244 \quad M = \sum_{i=1}^n \hat{m}_i W_i(z) \quad (4.2b)$$

246 with expansion coefficients  $\hat{\eta}_{ij}$  and  $\hat{m}_i$  for  $\eta_j$  and  $M$ , respectively. By substituting Eq. (4.2a) into  
 247 Eq. (4.1), and by comparing this result with Eq. (4.2b), we find

$$248 \quad \hat{m}_i = \sum_{j=1}^n \tilde{m}_j \hat{\eta}_{ij} \quad (4.3)$$

249 and so the expansion coefficients,  $\tilde{m}_j$ , are determined by inverting the matrix  $\hat{\eta}_{ij}$ . In order for the  
 250 inverse to exist, the determinant of this matrix must be non-zero.

251 To investigate the structure of the matrix, we perform a singular vector decomposition:

$$252 \quad \hat{\eta}_{ij} = \sum_{k=1}^n \lambda_k w_{ik} \tilde{w}_{kj}, \quad (4.4)$$

253 with eigenvalues,  $\lambda_k$ , and eigenvectors,  $w_{ik}$  and  $\tilde{w}_{kj}$ , the subscript  $k$  designating the index for the  
 254 eigenmode. These are defined by linear eigenvalue problems:

$$255 \quad \sum_{j=1}^n \hat{\eta}_{ij} w_{jk} = \lambda_k w_{ik} \quad (4.5a)$$

$$256 \quad \sum_{i=1}^n \tilde{w}_{ki} \hat{\eta}_{ij} = \lambda_k \tilde{w}_{kj}. \quad (4.5b)$$

258 These two vector sets are called the right- and the left-vectors, which satisfy the orthonormality

$$259 \quad \sum_{k=1}^n \tilde{w}_{ik} w_{kj} = \delta_{ij}. \quad (4.6)$$

260 As a result, the determinant and the inverse matrix are defined by

$$261 \quad \det(\hat{\eta}_{ij}) = \prod_{k=1}^n \lambda_k, \quad (4.7a)$$

$$262 \quad \hat{\eta}_{ij}^{-1} = \sum_{k=1}^n \lambda_k^{-1} w_{ik} \tilde{w}_{kj}, \quad (4.7b)$$

263  
264 respectively. The eigenvalue spectrum,  $\{\lambda_k\}$ , characterizes a singularity of a given matrix. If any  
265 of the eigenvalues,  $\lambda_k$ , are too small, the determinant becomes very small, and the inverse matrix  
266 becomes singular.

267 Figure 8(a) and (b) shows the plume spectrum,  $\{\eta_j(z)\}$ , and the plume matrix,  $(\hat{\eta}_{ij})$ , respec-  
268 tively. To ensure that we retain sufficient vertical modes for the decomposition, and henceforth for  
269 the dimension of the matrix,  $(\hat{\eta}_{ij})$ , we re-set  $n = 40$  in Eq. (2.3) only for the analysis of the present  
270 subsection. The eigenvalues,  $\lambda_k$ , obtained by the singular vector decomposition of Eq. (4.4) are  
271 plotted in Fig. 9: note that we have chosen to label the eigenvectors in order of decreasing mag-  
272 nitude of the corresponding eigenvalues,  $|\lambda_k|$ . The eigenvalues fall to very small values above  
273  $k \geq 20$ , suggesting that the entraining plume decomposition is highly redundant, and as a result  
274 the determinant of the matrix,  $(\hat{\eta}_{ij})$ , practically vanishes.

275 However, the singular vector decomposition can be used to regularize a matrix by removing all  
276 the small eigenvalues,  $\lambda_k$ , with, say,  $k > n_c$  (with  $n_c < n$ ) from the summations in Eqs. (4.4) and  
277 (4.7b). Thus, we obtain

$$278 \quad \hat{\eta}_{ij} \simeq \sum_{k=1}^{n_c} \lambda_k w_{ik} \tilde{w}_{kj}, \quad (4.8a)$$

$$279 \quad \hat{\eta}_{ij}^{-1} \simeq \sum_{k=1}^{n_c} \lambda_k^{-1} w_{ik} \tilde{w}_{kj}. \quad (4.8b)$$

281 Setting  $n_c = 16$  yields a regularized matrix  $(\hat{\eta}_{ij})$  shown in Fig. 10(a), and its transformation back  
282 to real space leads to Fig. 10(b). The reconstruction is noisier than the original spectrum shown in  
283 Fig. 8(a); nevertheless, the overall structure remains surprisingly similar.

284 In summary, the completeness analysis demonstrates the entraining–plume decomposition to be  
 285 highly redundant, so that it does not directly permit a decomposition of any vertical mass flux  
 286 profile under the formulae (4.1) and (4.3) due to a singularity of the matrix,  $(\hat{\eta}_{ij})$ . However, the  
 287 singularity can easily be removed under a singular–vector decomposition, and the reconstructed  
 288 nonsingular plume spectrum remains fairly close to the original entraining–plume spectrum. Thus,  
 289 the redundancy of the entraining–plume decomposition is not a practical issue in applying the  
 290 convective quasi–equilibrium closure.

291 *b. Eigenvalues and eigenvectors of the interaction matrix,  $\mathbf{K}$*

292 The basic structure of the interaction matrix,  $\mathbf{K}$ , can also be elucidated by performing a singular–  
 293 vector decomposition. Here, the right– and the left–eigenvectors,  $\vec{\mathbf{M}}_l$  and  $\tilde{\mathbf{M}}_l$ , respectively, are  
 294 defined by solving linear eigenvalue problems:

$$295 \quad \mathbf{K}\vec{\mathbf{M}}_l = \kappa_l\vec{\mathbf{M}}_l, \quad (4.9a)$$

$$296 \quad \tilde{\mathbf{M}}_l\mathbf{K} = \kappa_l\tilde{\mathbf{M}}_l \quad (4.9b)$$

297  
 298 with the eigenvalues,  $\kappa_l$  ( $l = 1, \dots, n$ ). Recall the orthonormality:

$$299 \quad \tilde{\mathbf{M}}_i \cdot \vec{\mathbf{M}}_j = \delta_{ij}. \quad (4.10)$$

300 The large–scale forcing vector,  $\vec{\mathbf{F}}$ , may then be represented in terms of the interaction matrix  
 301 decomposition by

$$302 \quad \vec{\mathbf{F}} = \sum_l F_l \vec{\mathbf{M}}_l \quad (4.11)$$

303 with the expansion coefficients,  $F_l$ , being defined by

$$304 \quad F_l = \tilde{\mathbf{M}}_l \cdot \vec{\mathbf{F}}. \quad (4.12)$$

305 Similarly, the cloud–base mass–flux vector,  $\vec{\mathbf{M}}$ , may be represented as

$$306 \quad \vec{\mathbf{M}} = \sum_l \mu_l \vec{\mathbf{M}}_l. \quad (4.13)$$



307 Substitution of Eqs. (4.11) and (4.13) into Eq. (1.1) shows that the expansion coefficients are  
 308 related by

$$309 \mu_l = F_l / \kappa_l. \quad (4.14)$$

310 The interaction–matrix eigenvalues,  $\kappa_l$ , are plotted in Fig. 11 in decreasing order of their absolute  
 311 values. From Eq. (4.14), if the large–scale forcing were to contribute with the same order to all  
 312 of the eigenmodes [*cf.*, Fig. 1(b)], then the higher–order modes (say,  $l \geq 14$ ) would dominate the  
 313 convective response.

314 Considering the eigenmodes themselves, the spectra of the first eight right– and left–  
 315 eigenvectors,  $\vec{\mathbf{M}}_l$  and  $\tilde{\mathbf{M}}_l$ , are shown in Figs. 12 and 13, respectively. The most striking feature  
 316 is that the right eigenvectors,  $\vec{\mathbf{M}}_l$ , are dominated by the high–entrainment (*i.e.*, high mode index)  
 317 shallower modes, whereas the left–eigenvectors,  $\tilde{\mathbf{M}}_l$ , encompass relatively low–entrainment deep  
 318 modes (from the 8th to the 14th mode index).

319 These features have significant consequences in defining the response of convection,  $\vec{\mathbf{M}}$ , against  
 320 a given large–scale forcing,  $\vec{\mathbf{F}}$ . First, the expansion coefficients,  $F_l$ , for the large–scale forcing  
 321 are defined by projecting the large–scale forcing,  $\vec{\mathbf{F}}$ , onto the left–eigenvectors,  $\tilde{\mathbf{M}}_l$  by Eq. (4.12).  
 322 Since  $\tilde{\mathbf{M}}_l$  reflects the deeper modes, there is a tendency that the deeper the structure of the large–  
 323 scale forcing, the stronger the projection onto the expansion coefficients,  $F_l$ , and hence onto  $\mu_l$ ,  
 324 through Eq. (4.14). However, the right–eigenvectors,  $\vec{\mathbf{M}}_l$ , are dominated by the shallow modes,  
 325 and thus, the convective response,  $\vec{\mathbf{M}}$ , as defined by Eq. (4.13) is also dominated by shallow modes.  
 326 Due to these different characteristics of the left– and the right–eigenvectors, we therefore find that  
 327 convection responds most effectively to deeper modes of large–scale forcing, but that it manifests  
 328 as a response primarily through the shallower modes. Note that this “twisted” relation stems from  
 329 a strong asymmetry of the interaction matrix, as is demonstrated more explicitly using a simple  
 330 idealized example matrix in the next subsection.

331 *c. Analysis of an idealized, highly-truncated interaction matrix*

332 It is also informative to take an analytical perspective on the singularities in strict convective  
 333 quasi-equilibrium closure by examining an idealized interaction matrix, which captures its basic  
 334 characteristics. Specifically, we consider a  $3 \times 3$  interaction matrix,  $\mathbf{K}$ , of the form:

$$335 \quad \mathbf{K} = \begin{pmatrix} k & -k_d & -k_d \\ k_s & k & -k_d \\ k_s & k_s & -1 \end{pmatrix} \quad (4.15a)$$

336 The quasi-equilibrium closure of Eq. (1.1) reduces to:

$$337 \quad \mathbf{K} \begin{pmatrix} M_3 \\ M_2 \\ M_1 \end{pmatrix} + \begin{pmatrix} F_3 \\ F_2 \\ F_1 \end{pmatrix} = 0. \quad (4.15b)$$

338 Here, the order of the vector indices for  $\vec{\mathbf{M}}$  and  $\vec{\mathbf{K}}$  is reversed from a standard convention so that  
 339 the matrix form defined by Eq. (4.15a) closely follows the matrix-element distributions shown  
 340 in Fig. 4: the given distribution can directly be compared with the definition (4.15a) by flipping  
 341 the horizontal direction in the figures. The idealized matrix is normalized by setting the right-  
 342 lowest element to  $-1$ ;  $k$ ,  $k_s$ , and  $k_d$  are expected to be small values, where  $k$  and  $k_s$  represent  
 343 destabilization tendencies of shallow convection modes acting on themselves and on the deeper  
 344 modes, respectively, whereas  $-k_d$  represents the stabilization from the deeper modes to shallower  
 345 modes.

346 The solution to the matrix problem (4.15b) is:

$$347 \quad M_3 = [(2k - k_s + k_d - 1)k_s k_d - k^2]^{-1} [(k - k_s k_d)F_3 + (1 + k_s)k_d F_2 - (k + k_d)k_d F_1] \quad (4.16a)$$

$$348 \quad M_2 = [(2k - k_s + k_d - 1)k_s k_d - k^2]^{-1} [(k_d - 1)k_s F_3 + (k - k_s k_d)F_2 - (k - k_s)k_d F_1] \quad (4.16b)$$

$$349 \quad M_1 = [(2k - k_s + k_d - 1)k_s k_d - k^2]^{-2} [(k - k_s)k_s F_3 + (k + k_d)k_s F_2 - (k^2 + k_s k_d)F_1]. \quad (4.16c)$$

350

351 A further simplification is to set all the small parameters to the same value,  $k_s = k_d = k$ , so that  
 352 the solution in Eq. (4.16) becomes:

$$353 \quad M_3 = \frac{1}{2(k-1)k} [(1-k)F_3 + (1+k)F_2 - 2kF_1] \quad (4.17a)$$

$$354 \quad M_2 = \frac{F_3 - F_2}{2k} \quad (4.17b)$$

$$355 \quad M_1 = \frac{-F_2 + F_1}{1-k}. \quad (4.17c)$$

356

357 When the limit of  $k \rightarrow 0$  is taken, the above solution reduces to

$$358 \quad M_3 \rightarrow -\frac{F_3 + F_2}{2k}$$

$$359 \quad M_2 \rightarrow \frac{F_3 - F_2}{2k}$$

$$360 \quad M_1 \rightarrow -F_2 + F_1,$$

361

362 retaining only the leading terms with respect to  $k$ , and assuming all forcing components,  $F_j$  ( $j =$   
 363  $1, 2, 3$ ), to be of  $O(1)$ . Thus, the two shallowest convective modes,  $M_3$  and  $M_2$ , respectively, diverge  
 364 in the limit of  $k \rightarrow 0$ . Also note that the signs of  $M_2$  and  $M_1$  sensitively depend on differences  
 365 between  $F_3$  and  $F_2$ , and that between  $F_2$  and  $F_1$ , respectively.

366 In this manner, the idealized matrix (4.15a) provides a very simple demonstration for the origin  
 367 of the singular behaviors of the quasi-equilibrium closure that were seen in previous sections.

#### 368 *d. Perturbation Analysis*

369 The idealized matrix problem may be further developed by considering a perturbation expansion.

370 Noting that many of the matrix elements are small in  $\mathbf{K}$ , we can write:

$$371 \quad \mathbf{K} = \mathbf{K}^{(0)} + \delta\mathbf{K}^{(1)} \quad (4.18a)$$

$$372 \quad \vec{\mathbf{M}} = \vec{\mathbf{M}}^{(0)} + \delta\vec{\mathbf{M}}^{(1)} + \dots \quad (4.18b)$$

373

374 where  $\delta$  is a small expansion parameter, and where the idealized matrix of Eq. (4.15a) can be  
 375 decomposed as:

$$376 \quad \mathbf{K}^{(0)} = \begin{pmatrix} 0 & 0 & 0 \\ 0 & 0 & 0 \\ 0 & 0 & 1 \end{pmatrix} \quad (4.19a)$$

$$377 \quad \delta \mathbf{K}^{(1)} = \begin{pmatrix} k & -k_d & -k_d \\ k_s & k & -k_d \\ k_s & k_s & 0 \end{pmatrix} \quad (4.19b)$$

378  
 379 To  $O(1)$ , we obtain:

$$380 \quad \mathbf{K}^{(0)} \vec{\mathbf{M}}^{(0)} + \vec{\mathbf{F}} = 0$$

381 with  $\det(\mathbf{K}^{(0)}) = 0$ , because of the fact that large elements are localized, and hence there is no  
 382 solution available for  $\vec{\mathbf{M}}^{(0)}$ . To avoid this problem, we need to re-formulate the expansion of  
 383 Eq. (4.18b) as:

$$384 \quad \vec{\mathbf{M}} = \frac{1}{\delta} \vec{\mathbf{M}}^{(-1)} + \vec{\mathbf{M}}^{(0)} + \dots \quad (4.20)$$

385 so that we obtain to  $O(1/\delta)$ :

$$386 \quad \mathbf{K}^{(0)} \vec{\mathbf{M}}^{(-1)} = 0, \quad (4.21)$$

387 which, with the matrix (4.15a), leads to

$$388 \quad M_1^{(-1)} = 0$$

389 and leaves the other two components,  $M_2^{(-1)}$  and  $M_3^{(-1)}$ , as undetermined. At  $O(1)$  we have,

$$390 \quad \mathbf{K}^{(0)} \vec{\mathbf{M}}^{(0)} + \mathbf{K}^{(1)} \vec{\mathbf{M}}^{(-1)} + \vec{\mathbf{F}} = 0, \quad (4.22)$$

391 which makes the problem solvable. Specifically for the case with Eq. (4.15a), this  $O(1)$  relation  
 392 defines  $M_2^{(-1)}$ ,  $M_3^{(-1)}$ , and  $M_1^{(0)}$ .

393 Thus, the perturbation analysis here more explicitly demonstrates how a strict application of the  
394 convective quasi-equilibrium condition tends to lead to an abnormally strong response of shallow  
395 convection to large-scale forcing.

## 396 **5. Physical Implications**

397 The present paper has focused on a rather narrow question of mathematical difficulties with  
398 the original closure formulation of Arakawa and Schubert (1974). In concluding, we turn to the  
399 physical implications from the present findings, also referring to background issues.

### 400 *a. Free-ride principle*

401 The convective quasi-equilibrium closure of Eq. (1.1) is based on stationarity of the cloud work  
402 function, which is a vertically-integrated quantity (*cf.*, Eq. 133 of Arakawa and Schubert 1974).  
403 Thus, the closure is also formulated in terms of vertically-integrated quantities. However, we  
404 might intuitively expect that a certain quasi-equilibrium state (*i.e.*, a balance condition) is achieved  
405 at each vertical level, at least to a good approximation, if a large enough number of convective  
406 modes is considered. The different modes provide different weighting functions and upper limits  
407 for the integrals in question.

408 It is observationally known that the large-scale tropical atmosphere satisfies a free-ride state  
409 (Fraedrich and McBride 1989; later Sobel *et al.* 2001 term it alternatively as “weak temperature  
410 gradient”), with a close balance between the large-scale tendency and the convective response in  
411 both the heat and moisture equations:

$$412 \quad w \frac{d\bar{\theta}}{dz} \simeq Q_1 + Q_R, \quad (5.1a)$$

$$413 \quad w \frac{d\bar{q}_v}{dz} \simeq -\frac{C_p}{L} Q_2. \quad (5.1b)$$

415 Here,  $Q_1$  and  $Q_2$  are tendencies due to non-advective processes, apart from radiative heating,  
416  $Q_R$ , in the context of large-scale modeling (*i.e.*, convective-scale advections are not explicitly

417 considered). See Fig. 1 of Yano (2001: also reproduced as Fig. 4.2 in Ch. 4 of Plant and Yano  
 418 2015) for a graphical demonstration. Although the literature tends to refer only to the balance  
 419 (5.1a), here, it is seen that the second balance (5.1b) is equally valid. In the large-scale tropical  
 420 atmosphere,  $Q_1$  and  $Q_2$  are mostly due to convection (*i.e.*,  $Q_c$ ). On the other hand, the vertical  
 421 advection and the radiation terms may be combined to define the total large-scale forcing,  $F_L$ .  
 422 Thus, the free-ride state may be equivalently expressed in the form

$$423 \quad Q_c + F_L \simeq 0 \quad (5.2)$$

424 for both variables. Eq. (5.2) may be considered as a statement of convective quasi-equilibrium,  
 425 but defined separately on each vertical level, rather than as an integral constraint.

426 Hence, we are led to ask whether, given enough plume modes in Eq. (1.1), we obtain a free-  
 427 ride state corresponding to Eq. (5.2): will this be actually accomplished in practice by the quasi-  
 428 equilibrium closure?

#### 429 *b. Completeness of the plume spectrum*

430 Equivalence between Eqs. (1.1) and (5.2) could be established if the mass–flux spectrum were  
 431 able to represent any possible convective response that may be required to satisfy the free–ride  
 432 state. Thus, a first consideration is whether the mass–flux spectrum is flexible enough to represent  
 433 any possible vertical profile. This has been examined using normal–mode and singular–vector de-  
 434 compositions in Sec. 4.a. The entraining–plume decomposition is shown to be highly redundant,  
 435 as expected from the individual plume profiles (*cf.*, Fig. 2), and so a decomposition of the entrain-  
 436 ing plumes into normal modes does not provide well–defined expansion coefficients. However,  
 437 this ill-posedness of the decomposition can be resolved by removing all the singular vectors with  
 438 almost–vanishing eigenvalues from the expansion. A reconstructed plume spectrum still remains  
 439 fairly close to the original entraining–plume spectrum, but practically removing the redundancy.

440 Here, the mathematical question of the completeness of a plume spectrum addresses its capacity  
441 and flexibility to represent any physically-feasible vertical structure of convection. As we have  
442 seen, the conclusion obtained is rather mixed, and further investigations from a more practical  
443 perspective could be warranted.

444 *c. Convective response under the spectrum mass flux*

445 The next consideration is how an individual plume mode modifies the large-scale thermody-  
446 namic state (*i.e.*, convective response: Sec. 3.b). The effect of an individual entraining plume  
447 is comprised of two main parts: (i) detrainment that cools and moistens the large-scale by re-  
448 evaporation of the detrained cloudy air; and, (ii) compensating environmental descent, in response  
449 to the convective updraft, that induces adiabatic heating and drying. A major difference between  
450 these two effects is that the detrainment effect is found only at a single level at the plume top,  
451 whereas the environmental descent is felt at all of the vertical levels spanned by the plume. As a  
452 result, the detrainment effect focused on a single vertical level tends to be abnormally strong, with  
453 cooling and moistening rates far exceeding  $10 \text{ Kday}^{-1}$  and so strongly dominant at that level over  
454 the environmental-descent effect.

455 The consequence is that a straightforward inversion of the interaction matrix in the closure con-  
456 dition of Eq. (1.1) produces a full convective response against a given large-scale forcing that be-  
457 comes very singular (Sec. 3.c). For idealized large-scale forcing profiles with a half-sine shaped  
458 large-scale uplifting, we find that the convective response is dominated by singularly strong warm-  
459 ing and cooling induced at the top of the detraining-plume downdrafts (*i.e.*, entraining-plume  
460 updraft modes with a negative amplitude). Due to the tendency of entraining-plume modes to pro-  
461 duce a singular response, the convective quasi-equilibrium closure condition does not achieve a  
462 thermodynamic state close to the free ride balances. Thus, the mathematical analysis herein points

463 out in an explicit manner how and why a physically unrealistic feature of the entraining–plume  
464 model causes a problem.

465 A very simple way of removing these singular cooling–moistening effects would be to neglect  
466 all of the detrainment effects from the interaction matrix,  $\mathbf{K}$ , by setting  $\mathbf{K}_d = 0$  in Eq. (3.1) so  
467 that the interaction matrix,  $\mathbf{K}$ , is replaced by  $\mathbf{K}_v$ . However, totally removing this effect from the  
468 convective equilibrium problem would not be very realistic for reasons discussed in Sec. 4.e.

#### 469 *d. Interaction matrix analysis*

470 Another important aspect of the convective response under the convective quasi–equilibrium  
471 closure is the dominance of shallow plumes regardless of the vertical extent of large–scale forcing.  
472 This is rather unintuitive. However, one must remember that as a matter of principle, large–scale  
473 forcing is projected to all the plume modes by design, as explicitly shown by Fig. 1(a). The  
474 resulting spectrum of the convective response is rather nontrivial, mathematically taking the form  
475 of a matrix inversion. This character of the problem means that we need to pay attention to the  
476 mathematical behaviour of the inversion calculation in order to better understand the structural  
477 issues involved.

478 First, a singular–vector decomposition is performed on the interaction matrix in Sec. 4.b. The  
479 left–eigenvector spectra are dominated by middle–height plume modes, with maximum heights  
480 of 8–10 km, thus relatively deep components of large–scale forcing lead to a strong response by  
481 convection. On the other hand, the right–eigenvector spectra are dominated by shallow plume  
482 modes, and thus relatively–deep large–scale forcing modes are strongly projected onto shallow  
483 convective modes.

484 This rather strong asymmetry between the left and the right eigenvectors stems from a strong  
485 asymmetry in the interaction matrix itself. In turn, the asymmetry of the interaction matrix stems  
486 from the nature of the detrainment effect of a plume mode onto other plume modes: only the



487 deeper plume modes are affected by detrainment from a given plume mode, and this gives rise to  
488 the triangular structure apparent within the interaction matrix (*cf.*, Fig. 4(b)).

489 With increasing precipitating efficiency, the detrainment effect becomes weaker as less cloudy  
490 air is available to detrain at plume top. In a fully-precipitating limit for all of the plume modes,  
491 then the asymmetry of the interaction matrix would disappear, and the singular response to the  
492 large-scale forcing would be removed. However, additional calculations (not shown) indicate that  
493 even a weak asymmetry of the interaction matrix can lead to a singular response. A relatively  
494 strong sensitivity of the convective response to the transition scale,  $\epsilon_0$ , in precipitation-efficiency  
495 [Eq. (2.5)] has also been found because this parameter controls the relative contribution of detrain-  
496 ment effects to the interaction matrix.

497 An idealized  $3 \times 3$  interaction matrix (Sec. 4.c-d) is able to reproduce the character of these  
498 results. A singular perturbation expansion is required for describing the convective quasi-  
499 equilibrium closure due the fact that the matrix elements related to shallow convection tend to  
500 be substantially smaller than those for the interactions between deep convection. As a result,  
501 shallow convection tends to respond to large-scale forcing in a singular manner.

#### 502 *e. Further Physical Implications*

503 An important feature throughout the present analysis is the strong cooling and moistening in-  
504 duced by re-evaporation of the detrained cloudy air. When this contribution is suppressed, the con-  
505 vective response under the quasi-equilibrium closure becomes much more reasonable. It is worth  
506 noting that some alternative formulations of mixing, beyond the simple entrainment formulation  
507 of pure Arakawa and Schubert (1974), may help to alleviate the problem (de Rooy *et al.* 2013,  
508 Yano 2015). Another legitimate way of suppressing this effect is to couple the convection param-  
509 eterization with a stratiform cloud representation, and to transfer the detrained cloudy convective  
510 air to form part of a stratiform cloud rather than immediately re-evaporating it into the environ-

511 ment. The importance of this procedure would probably be needless to emphasize, because such a  
512 coupling of convection with stratiform clouds is already accomplished in most of the operational  
513 global models already. However, its significance, to the extent revealed here, appears to be not  
514 widely appreciated.

515 At the same time, completely suppressing the evaporative cooling of the detrained cloudy air  
516 would likely not be wise. Yano and Plant (2012b) suggest that the resulting destabilization ten-  
517 dency of shallow convection can be a key mechanism driving transformations from shallow to  
518 deep convection. Two solutions may be considered for this remedy. The first is to retain the ten-  
519 dency explicitly for shallow convection, rather than imposing a strict equilibrium constraint. In  
520 this case, a singular response of shallow convection to large-scale forcing associated with evap-  
521 orative cooling must be tamed in a different manner. The second is to transfer the role of this  
522 destabilization tendency to the stratiform cloud scheme: the mechanism may be represented by  
523 the cloud-top entrainment process (*cf.*, Deardorff 1980, Randall 1980) under this reformulation,  
524 which is also expected to lead to an equivalent destabilization.

525 Another important implication from the present study is a much slower response time scale  
526 for the shallower convective modes than for the deep convection, as indicated by the relatively  
527 small elements in the interaction matrix. This implication can be seen directly from the prognostic  
528 equation for the cloud work function spectrum,  $\vec{\mathbf{A}}$ , from which the quasi-equilibrium closure (1.1)  
529 is derived:

$$530 \quad \frac{\partial \vec{\mathbf{A}}}{\partial t} = \mathbf{KM} + \vec{\mathbf{F}}. \quad (5.3)$$

531 The quasi-equilibrium closure has been justified based on an argument that an *overall* time scale  
532 for the response of convection to large-scale forcing is so short that we can drop the time tendency  
533 of the cloud work function on the left hand side, which is expected to evolve by following a slow  
534 large-scale time scale.

535 However, more precisely, the response time scale is short only for deep convection, but *not*  
536 for shallow convection. As a result, Eq. (5.3) may be approximated by Eq. (1.1) for the deep  
537 convection part only. In other words, the full convective ensemble does not immediately respond  
538 to any slow large-scale forcing, as originally envisioned by Arakawa and Schubert (1974). Rather,  
539 a finite time-scale for the convective response to large-scale forcing should explicitly be taken into  
540 account by retaining the temporal tendency of the cloud work function on the left hand side of  
541 Eq. (5.3), so that the closure becomes fully prognostic. Suitable formulations are already in place  
542 (*e.g.*, Pan and Randall 1998, Yano and Plant 2012c). Here, we point out a solid reason for moving  
543 towards this direction.

544 The issues appear to be further involved, because observational analyses by Zhang (2002, 2003),  
545 Donner and Phillips (2003) suggest that the boundary-layer processes controlling the evolution of  
546 the convective available potential energy (CAPE), and thus also likely of the cloud work functions,  
547 are of a much shorter time scale than those found in the free atmosphere. Thus, boundary-layer  
548 processes, neglected in the analysis herein, may further contribute to break down a strict applica-  
549 tion of convective quasi-equilibrium closure. Those implications warrant further investigations.

550 The present study further suggests needs for re-considering the mass-flux convection param-  
551 eterization formulation from more general perspectives. Such investigations are already under  
552 way (*e.g.*, Yano *et al.* 2005b, Yano 2014b, 2016). These developments should more seriously be  
553 considered in operational contexts.

## 554 **Appendix: Scale Analysis**

555 The purpose of this Appendix is to estimate the order of magnitude of cooling and moistening  
556 associated with re-evaporation of the detrained cloudy air.

We begin with the simple point that latent heating due to the condensation of a unit of water vapor,  $q = 1 \text{ g kg}^{-1}$ , leads to an increase of temperature by

$$qL/C_p = 2.5 \text{ K}$$

using the latent heating,  $L = 2.5 \times 10^6 \text{ J kg}^{-1}$ , and the specific heat capacity,  $C_p = 10^3 \text{ J kg}^{-1} \text{ K}^{-1}$  for air at constant pressure. A typical mass flux value under convective quasi-equilibrium is  $M \sim 10^{-2} \text{ kg m}^{-2} \text{ s}^{-1}$ , or  $M/\rho \sim w_0 = 10^{-2} \text{ ms}^{-1}$  in units of vertical velocity. At the convective cloud top, all of the mass flux detrains under the entraining-plume hypothesis. The associated heat flux is thus

$$(M/\rho)(q_c L/C_p) \sim 2.5 \times 10^{-2} \times q_c \text{ K m s}^{-1} \sim 2.5 \times 10^3 \times q_c \text{ K m day}^{-1} \quad (\text{A.1})$$

557 where the detrained cloud-water mixing ratio,  $q_c$ , is expressed in units of [g/kg]. If the detrainment  
 558 occurs over a layer of, say, 1 km in depth, it will amount to a cooling rate of  $2.5 \text{ K day}^{-1}$  for  
 559  $q_c = 1 \text{ g kg}^{-1}$ .

The last piece of estimate is the amount of cloud water,  $q_c$ , expected at the convective cloud top at the height of, say,  $H \sim 10 \text{ km}$ . To obtain this, we note that within a convective updraft, condensative heating is well balanced by adiabatic cooling (a local realization of free-ride state: *cf.*, Eq. 5.1). Thus,

$$\frac{L}{C_p} \frac{dq_v^*}{dz} + \frac{d\theta}{dz} \simeq 0.$$

This relation leads to an estimate for the rate of decrease of saturated water-vapor with height,

$$\frac{dq_v^*}{dz} \sim -\frac{C_p}{L} \frac{d\theta}{dz} \sim -10^{-6} \text{ m}^{-1}.$$

Thus, neglecting fall out due to precipitation, the accumulation of condensed water in lifting through a height  $H \sim 10 \text{ km}$  is estimated as:

$$q^* = -H \frac{dq_v^*}{dz} \sim 10^{-6} \text{ m}^{-1} \times 10^4 \text{ m} \sim 10^{-2} \text{ kg kg}^{-1} \sim 10 \text{ g kg}^{-1}. \quad (\text{A.2})$$

560 Substitution of Eq. (A.2) into Eq. (A.1) leads to an estimate of the cooling rate of  $25 \text{ K day}^{-1}$  for  
561 a 1 km–deep detrainment layer.

562 **References**

- 563 Arakawa, A., and W. H. Schubert, 1974: Interaction of a cumulus cloud ensemble with the large-  
564 scale environment, Part I. *J. Atmos. Sci.*, **31**, 674–701.
- 565 Bechtold, P., N. Semane, P. Lopez, J.-P. Chaboureau, A. Beljaars, N. Bormann, 2014: Repre-  
566 senting equilibrium and non-equilibrium convection in large-scale models. *J. Atmos. Sci.*, **71**,  
567 734–753.
- 568 Deardorff, J. W., 1980: Cloud top entrainment instability. *J. Atmos. Sci.*, **37**, 131–147.
- 569 de Rooy, Wim C., Bechtold, P., Frohlich, K., Hohenegger, C., Jonker H., Mironov, D., Pier  
570 Siebesma, A., Teixeira, J., and Yano, J.-I., 2013: Entrainment and detrainment in cumulus convec-  
571 tion: an overview. *Quart. J. Roy. Meteor. Soc.*, **139**, 1–19, DOI: 10.1002/qj.1959.
- 572 Donner, L. J. and V. T. Phillips, 2003: Boundary layer control on convective available po-  
573 tential energy: implications for cumulus parameterization, *J. Geophys. Res.*, **108**, 4701,  
574 doi:10.1029/2003JD003773.
- 575 Fraedrich, K., and J. L. McBride, 1989: The physical mechanism of CISK and the free-ride bal-  
576 ance. *J. Atmos. Sci.*, **46**, 2642–2648.
- 577 Fulton, S. R., and W. H. Schubert, 1985: Vertical normal mode transforms: Theory and applica-  
578 tion. *Mon. Wea. Rev.*, **113**, 647–658.
- 579 Hack, J. J., W. H. Schubert, and P. L. Silva Dias, 1984: A spectral cumulus parameterization for  
580 use in numerical models of tropical atmosphere. *Mon. Wea. Rev.*, **112**, 704–716.
- 581 Houze, R. A., Jr., and A. K. Betts, 1981: Convection in GATE, *Rev. Geophys. Space Phys.*, **19**,  
582 541–576.
- 583 Jordan, C. L., 1958: Mean sounding for the West Indies area. *J. Meteor.*, **15**, 91–97.

584 Kasahara, A., and K. Puri, 1981: Spectral representation of three-dimensional global data by  
585 expansion in normal mode functions. *Mon. Wea. Rev.*, **109**, 37–51.

586 Lord, S. J., 1982: Interaction of a cumulus cloud ensemble with the large-scale environment. Part  
587 III: Semi-prognostic test of the Arakawa-Schubert cumulus parameterization. *J. Atmos. Sci.*, **39**,  
588 88–103.

589 Lord, S. J., and A. Arakawa, 1980: Interaction of a cumulus cloud ensemble with the large-scale  
590 environment, Part II. *J. Atmos. Sci.*, **37**, 2677–2692.

591 Lord, S. J., W. C. Chao and A. Arakawa, 1982: Interaction of a cumulus cloud ensemble with the  
592 large-scale environment, Part IV. *J. Atmos. Sci.*, **39**, 104–113.

593 Mapes, B. E.: 1997: Equilibrium vs. activation controls on large-scale variations of tropical deep  
594 convection, in: *The Physics and Parameterization of Moist Atmospheric Convection*, R. K. Smith  
595 (Ed.), NATO ASI, Kloster Seeon, Kluwer Academic Publishers, Dordrecht, 321–358.

596 Moorthi, S., and M. J. Suarez, 1992: Relaxed Arakawa-Schubert. A parameterization of moist  
597 convection for general circulation models. *Mon. Wea. Rev.*, **120**, 978–1002.

598 Pan, D.-M., and D. A. Randall, 1998: A cumulus parameterization with prognostic closure, *Quart.*  
599 *J. Roy. Meteor. Soc.*, **124**, 949–981.

600 Plant, R. S., and J.-I. Yano (Eds), 2015: *Parameterization of Atmospheric Convec-*  
601 *tion*, Volumes I and II, World Scientific, Singapore, Imperial College Press, London  
602 <http://www.worldscientific.com/worldscibooks/10.1142/p1005>

603 Randall, D. A., 1980: Conditional instability of the first kind upside down. *J. Atmos. Sci.*, **37**,  
604 125–130.

605 Sobel, A. H., J. Nilsson, and L. M. Polvani, 2001: The weak temperature gradient approximation  
606 and balanced tropical moisture waves. *J. Atmos. Sci.*, **58**, 3650–3665.

607 Yano, J.-I., 2001: Residual cumulus parameterization. *Quart. J. Roy. Meteor. Soc.*, **127**, 1261–  
608 1276.

609 Yano, J.-I., 2014a: Basic Convective Element: Bubble or Plume?: A Historical Review. *Atmos.*  
610 *Phys. Chem.*, **14**, 7019–7030, doi:10.5194/acp-14-7019-2014

611 Yano, J.-I., 2014b: Formulation structure of mass-flux convection parameterization. *Dyn. Atmos.*  
612 *Ocean*, **67**, 1–28. <http://dx.doi.org/10.1016/j.dynatmoce.2014.04.002>

613 Yano, J.-I., 2015: Thermodynamic effects of convection under the mass–flux formulation, in:  
614 *Parameterization of Atmospheric Convection*, Volume I (R. S. Plant and J. I. Yano, Eds.), World  
615 Scientific, Imperial College Press, 227–248.

616 Yano, J. I., 2016: Subgrid–Scale Physical Parameterization in Atmospheric Modelling: How  
617 Can We Make it Consistent? *J. Phys. A: Math. Theor.*, **49**, 284001 doi:10.1088/1751-  
618 8113/49/28/284001.

619 Yano, J.-I., and R. S. Plant, 2012a: Convective quasi–equilibrium. *Rev. Geophys.*, **50**, RG4004,  
620 doi:10.1029/2011RG000378.

621 Yano, J.-I., and R. S. Plant, 2012b: Interactions between shallow and deep convection under a  
622 finite departure from convective quasi–equilibrium. *J. Atmos. Sci.*, **69**, 3463–3470.

623 Yano, J.-I., and R. S. Plant, 2012c: Finite Departure from Convective Quasi-Equilibrium: Periodic  
624 Cycle and Discharge-Recharge Mechanism. *Quart. J. Roy. Meteor. Soc.*, **138**, 626–637.

625 Yano, J.-I., and R. S. Plant, 2016: Generalized Convective Quasi-Equilibrium Principle. *Dyn.*  
626 *Atmos. Ocean.*, **73**, 10–33.



- 627 Yano, J.-I., J.-P. Chaboureau, and F. Guichard, 2005a: A generalization of CAPE into potential-  
628 energy convertibility. *Quart. J. Roy. Meteor. Soc.*, **131**, 861–875.
- 629 Yano, J.-I., J.-L. Redelsperger, F. Guichard, and P. Bechtold, 2005b: Mode decomposition as a  
630 methodology for developing convective-scale representations in global models. *Quart. J. Roy.*  
631 *Meteor. Soc.*, **131**, 2313–2336.
- 632 Yano J.-I., M. Bister, Z. Fuchs, L. Gerard, V. Phillips, S. Barkidija, and J. M. Piriou, 2013: Phe-  
633 nomenology of convection-parameterization closure, *Atmos. Phys. Chem.*, **13**, 4111–4131.
- 634 Zhang, G. J., 2002: Convective quasi-equilibrium in midlatitude continental environment and its  
635 effect on convective parameterization, *J. Geophys. Res.*, **107**, 4220, doi:10.1029/2001JD001005.
- 636 Zhang, G. J., 2003: The concept of convective quasi-equilibrium in the tropical western Pa-  
637 cific: Comparison with midlatitude continental environment. *J. Geophys. Res.*, **108**, 4592,  
638 doi:10.1029/2003JD003520.

639 **LIST OF FIGURES**

640 **Fig. 1.** The three types of the large-scale forcing profile considered; deep (solid, chain-dash), shallow (long-dash, double dotted-dash), and very shallow (short-dash, triple dotted-dash). In (a), the forcings are shown as a function of height for both the thermal (negative curves) and the moisture (positive curves) terms. In (b), the forcings are shown in terms of the generation rate of cloud-work function (as found in Eq. (1.1) across the spectrum of fractional entrainment rates. . . . . 34

646 **Fig. 2.** Normalized mass-flux profiles,  $\eta = M(z)/M(z_B)$ , for selected entraining plumes under the microphysical formulation given by Eq. (2.5). In order from the deepest (solid) to the shallowest profiles (double-dot chain), the plots are for values of  $\varepsilon = 1 \times 10^{-5}$ ,  $2 \times 10^{-5}$ ,  $4 \times 10^{-5}$ ,  $6 \times 10^{-5}$ , and  $8 \times 10^{-5} \text{ m}^{-1}$ . . . . . 35

650 **Fig. 3.** Dependence of the precipitation efficiency,  $c_0$ , on the fractional entrainment rate,  $\varepsilon$ , as defined by Eq. (2.5). . . . . 36

652 **Fig. 4.** The interaction matrix,  $\mathbf{K}_{ij}$ , is plotted with the index  $i$  shown vertically and  $j$  horizontally for corresponding fractional entrainment rates  $\varepsilon$  and  $\varepsilon'$  respectively, as defined by Eq. 2.3. The full matrix is shown in (a), and the two components due to detrainment and environmental descent are shown in (b) and (c) respectively. The evaluation uses the deep large-scale forcing (solid and chain-dash curves in Fig. 1). . . . . 37

657 **Fig. 5.** Profiles of the tendencies of (a) the temperature and (b) the moisture (mixing ratio) produced by convective plumes for given, selected entrainment rates:  $\varepsilon = 2 \times 10^{-5}$  (solid),  $4 \times 10^{-5}$  (long dash),  $6 \times 10^{-5}$  (short dash),  $8 \times 10^{-5} \text{ m}^{-1}$  (chain dash). Plotted in unit of K/day, also assuming the convective mass-flux amplitude of  $M_i = 10^{-2} \text{ kg m}^{-2} \text{ s}^{-1}$ . . . . . 38

661 **Fig. 6.** (a) The spectrum of convective-base mass-flux as a function of the fractional entrainment rate, as obtained from inverting the matrix,  $\mathbf{K}$ , in Eq. (1.1). Results are presented for the deep (solid), shallow (long-dashed), and very shallow (short-dashed) forcings, as shown in Fig. 1. (b) The corresponding vertical profiles of the total mass flux. . . . . 39

665 **Fig. 7.** Vertical profiles of the convective tendencies for (a) temperature and (b) moisture (the mixing ratio) for the three large-scale forcing profiles given in Fig. 1: deep (solid), shallow (long-dashed), and very shallow (short-dashed). . . . . 40

668 **Fig. 8.** (a) The vertical profiles for the plume spectrum,  $\{\eta_j(z)\}$ , shown as a function of height (horizontal axis) and the plume index (vertical axis). (b) The plume matrix (*i.e.*, the spectrum of plumes decomposed by the vertical-velocity normal modes),  $\hat{\eta}_{ij}$ , shown as a function of the normal mode index  $i$  (horizontal axis) and the plume-type index  $j$  (vertical axis). See Eq. (4.2a) for its definition. . . . . 41

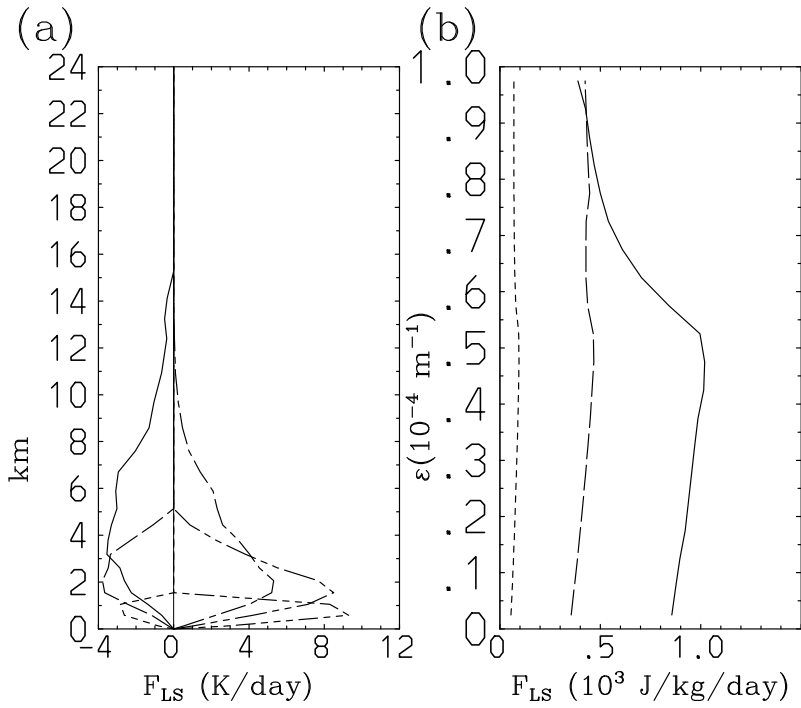
673 **Fig. 9.** The eigenvalues,  $\lambda_k$ , for the plume matrix,  $\hat{\eta}_{ij}$ , plotted as a function of the index,  $k$ , in decreasing order of their absolute value. Both the real (solid) and imaginary (long-dash) parts are shown. . . . . 42

676 **Fig. 10.** (a) The plume matrix,  $\hat{\eta}_{ij}$ , as in Fig. 8(b), but here following a regularization by retaining only the first  $n_c = 16$  modes in Eq. (4.4). (b) The vertical profiles for the plume spectrum,  $\{\eta_j(z)\}$ , as in Fig. 8(a), but reconstructed after the matrix regularization as in (a). Although both spectra contain complex values, only the real components are shown, the imaginary components being numerically negligible. . . . . 43

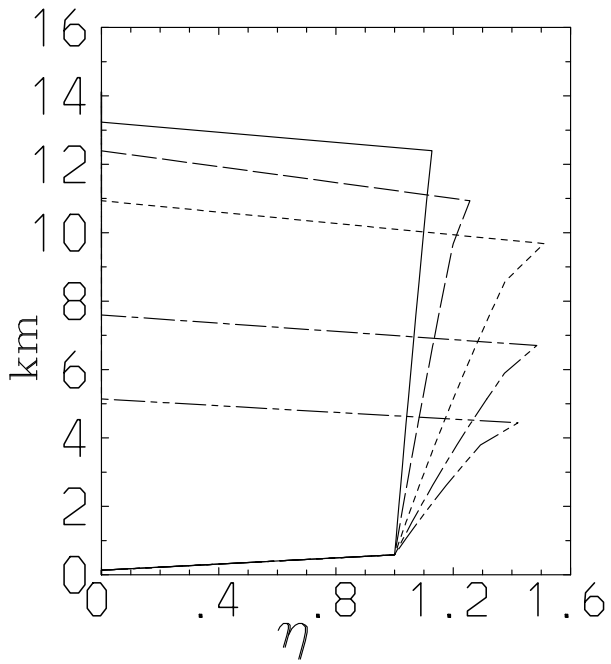
681 **Fig. 11.** The eigenvalues,  $\kappa_l$ , for the interaction matrix,  $\mathbf{K}$ , plotted as a function of the index,  $l$ , in de-  
 682 creasing order of their absolute value. Both the real (solid) and imaginary (long-dash) parts  
 683 are shown. An exceptionally large magnitude for the real component of the first eigenvalue  
 684 (less than  $-25$ ) is beyond the range of this plot and is not presented. The 2nd to the 9th  
 685 eigenvalues constitute a series of complex conjugate pairs, as well as the 11th and the 12th,  
 686 and from the 15th to the 18th. . . . . 44

687 **Fig. 12.** The first eight right-eigenvectors,  $\vec{\mathbf{M}}_l$  ( $l = 1, \dots, 8$ ), of the interaction matrix, as defined by  
 688 Eq. 4.9a. (a) Real and (b) imaginary components. The first four vectors are shown by solid,  
 689 long-dashed, short-dashed, and dot-dashed curves. They are followed by four other varying  
 690 types of the curves. Note that change of scale in the horizontal axis. . . . . 45

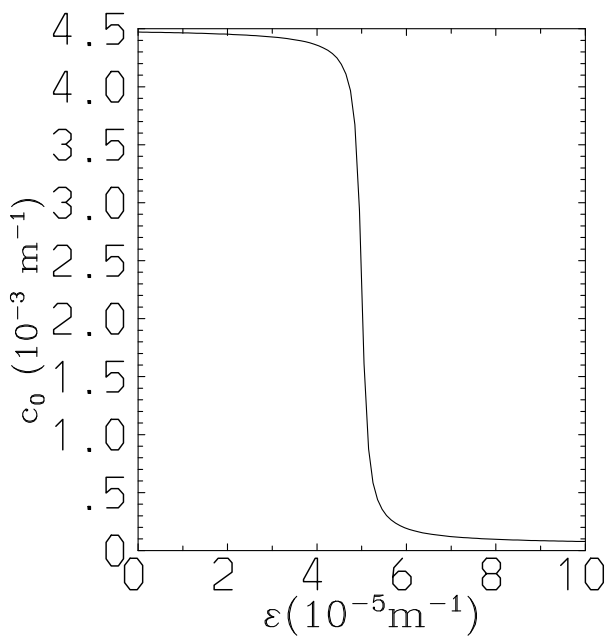
691 **Fig. 13.** The first eight left-eigenvectors,  $\tilde{\mathbf{M}}_l$  ( $l = 1, \dots, 8$ ), of the interaction matrix, as defined by  
 692 Eq. 4.9b. Plotted in the same format as for the right-eigenvectors in Fig. 12. . . . . 46



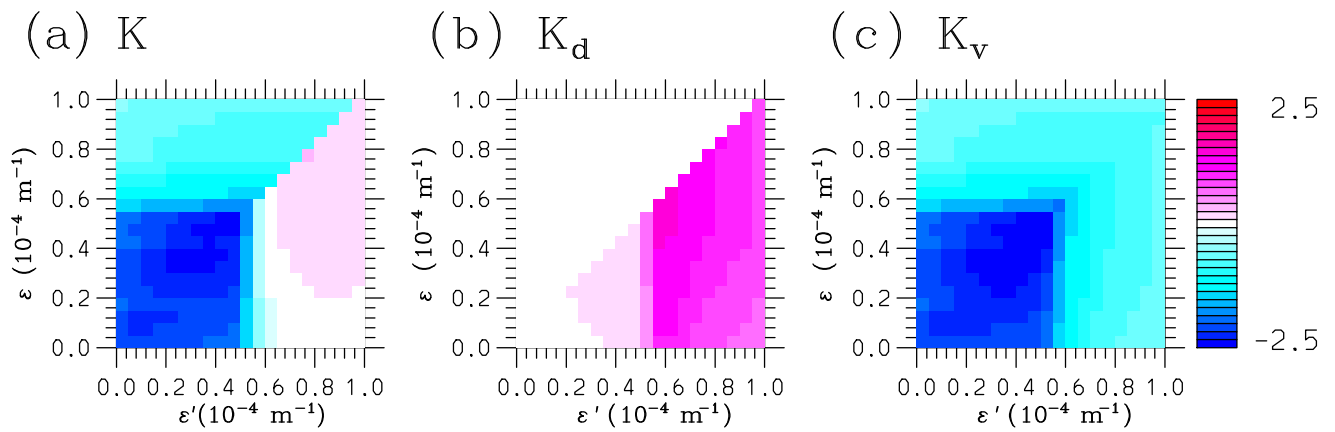
693 FIG. 1. The three types of the large-scale forcing profile considered; deep (solid, chain-dash), shallow (long-  
 694 dash, double dotted-dash), and very shallow (short-dash, triple dotted-dash). In (a), the forcings are shown  
 695 as a function of height for both the thermal (negative curves) and the moisture (positive curves) terms. In (b),  
 696 the forcings are shown in terms of the generation rate of cloud-work function (as found in Eq. (1.1)) across the  
 697 spectrum of fractional entrainment rates.



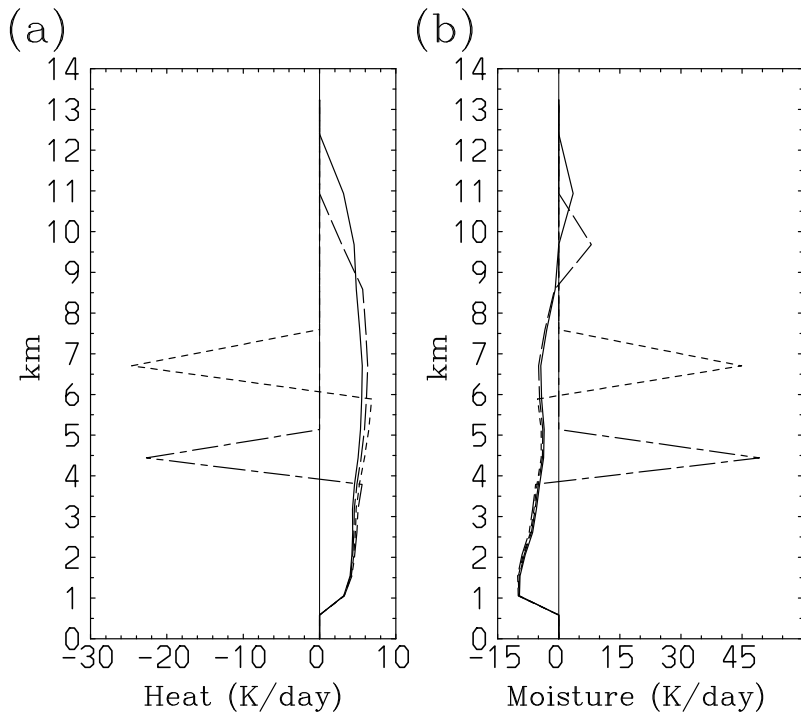
698 FIG. 2. Normalized mass-flux profiles,  $\eta = M(z)/M(z_B)$ , for selected entraining plumes under the micro-  
 699 physical formulation given by Eq. (2.5). In order from the deepest (solid) to the shallowest profiles (double-dot  
 700 chain), the plots are for values of  $\varepsilon = 1 \times 10^{-5}, 2 \times 10^{-5}, 4 \times 10^{-5}, 6 \times 10^{-5},$  and  $8 \times 10^{-5} \text{ m}^{-1}$ .



701 FIG. 3. Dependence of the precipitation efficiency,  $c_0$ , on the fractional entrainment rate,  $\epsilon$ , as defined by  
 702 Eq. (2.5).

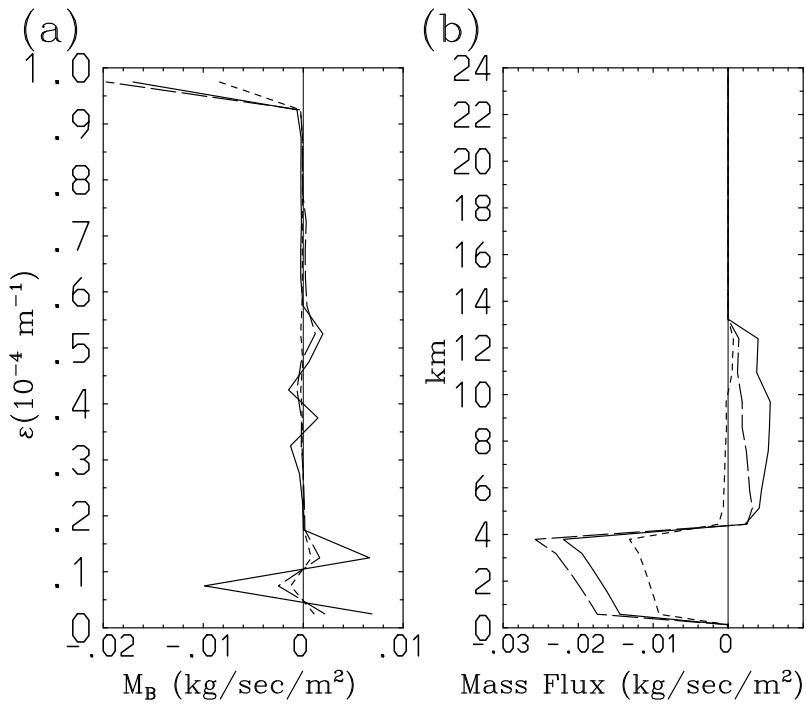


703 FIG. 4. The interaction matrix,  $\mathbf{K}_{ij}$ , is plotted with the index  $i$  shown vertically and  $j$  horizontally for corre-  
 704 sponding fractional entrainment rates  $\varepsilon$  and  $\varepsilon'$  respectively, as defined by Eq. 2.3. The full matrix is shown in  
 705 (a), and the two components due to detrainment and environmental descent are shown in (b) and (c) respectively.  
 706 The evaluation uses the deep large-scale forcing (solid and chain-dash curves in Fig. 1).

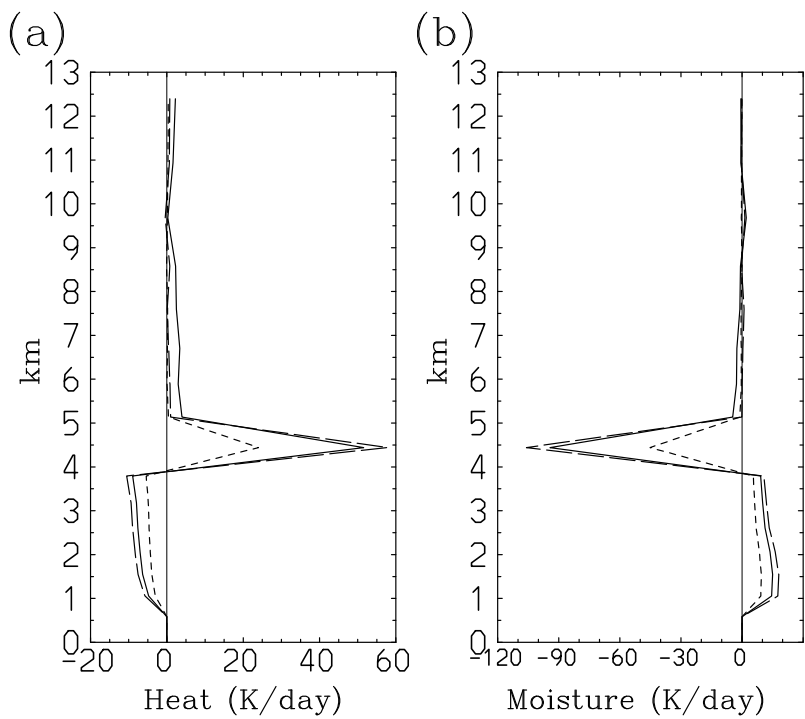


707 FIG. 5. Profiles of the tendencies of (a) the temperature and (b) the moisture (mixing ratio) produced by  
 708 convective plumes for given, selected entrainment rates:  $\epsilon = 2 \times 10^{-5}$  (solid),  $4 \times 10^{-5}$  (long dash),  $6 \times 10^{-5}$   
 709 (short dash),  $8 \times 10^{-5} \text{ m}^{-1}$  (chain dash). Plotted in unit of K/day, also assuming the convective mass-flux  
 710 amplitude of  $M_i = 10^{-2} \text{ kg m}^{-2} \text{ s}^{-1}$ .

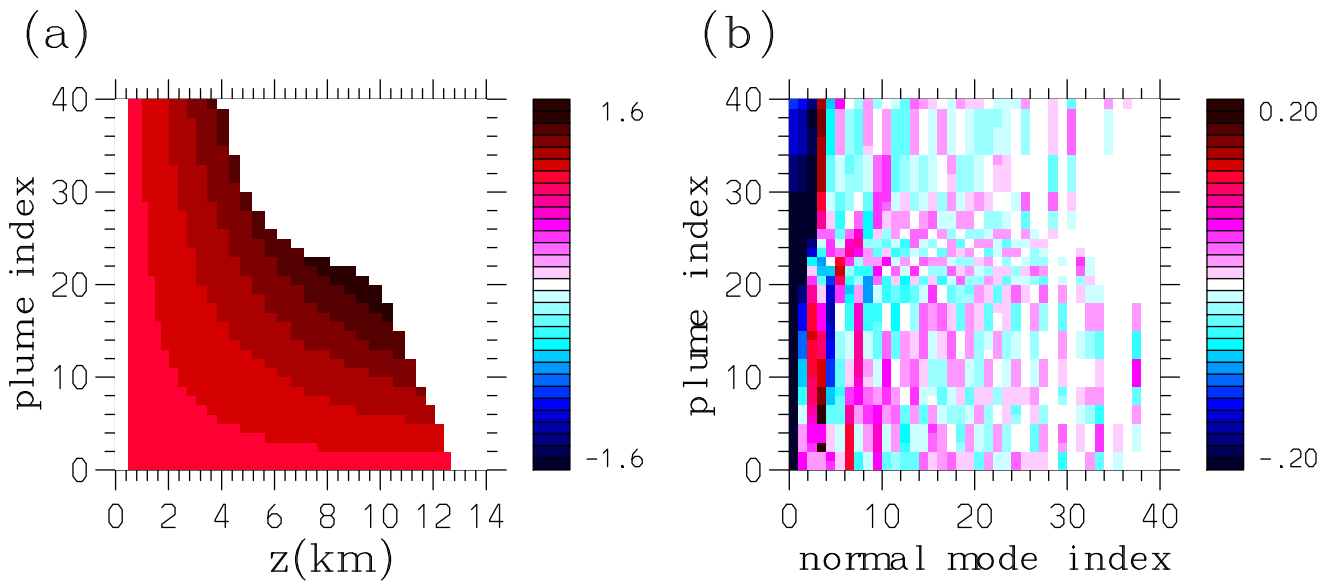




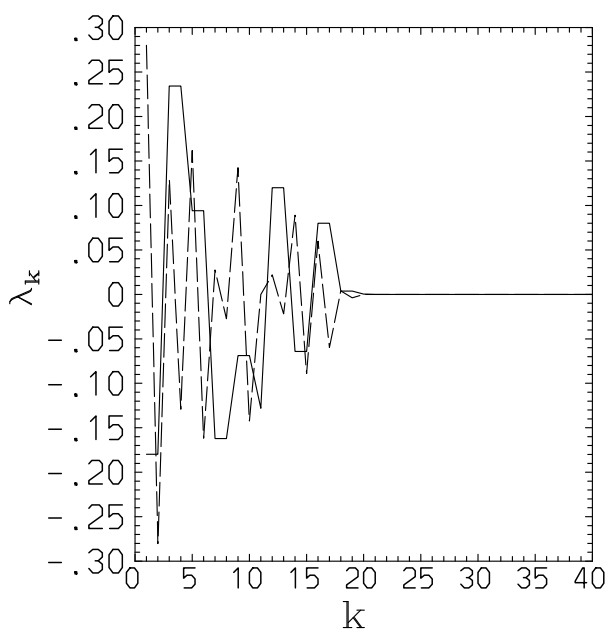
711 FIG. 6. (a) The spectrum of convective–base mass–flux as a function of the fractional entrainment rate, as  
 712 obtained from inverting the matrix,  $\mathbf{K}$ , in Eq. (1.1). Results are presented for the deep (solid), shallow (long–  
 713 dashed), and very shallow (short–dashed) forcings, as shown in Fig. 1. (b) The corresponding vertical profiles  
 714 of the total mass flux.



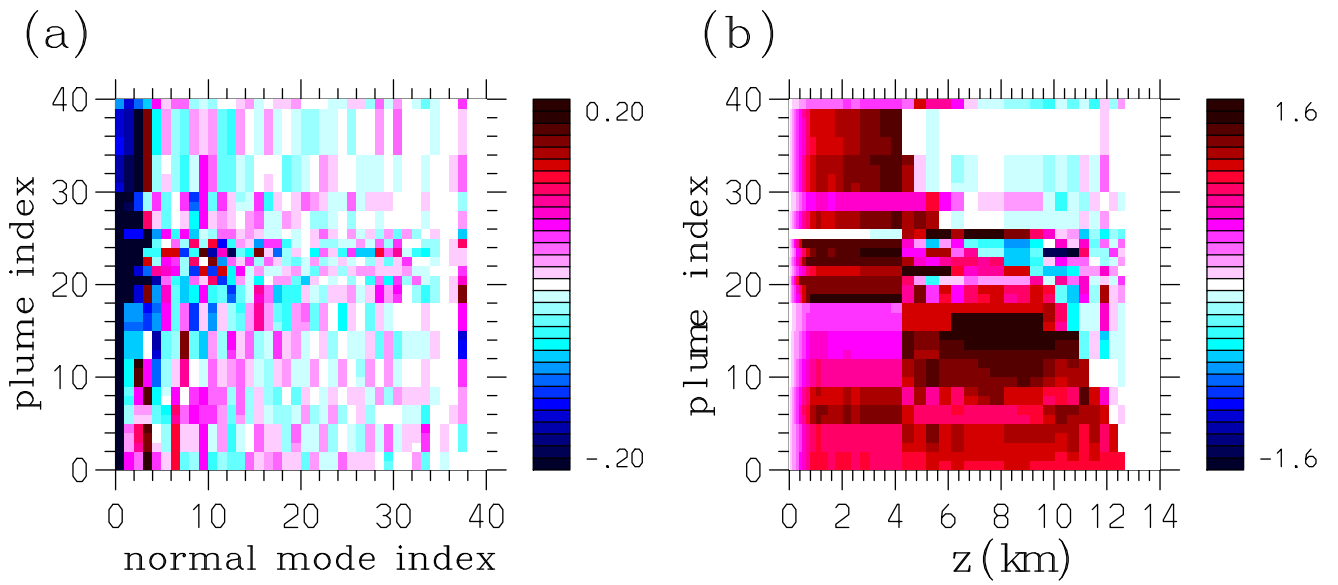
715 FIG. 7. Vertical profiles of the convective tendencies for (a) temperature and (b) moisture (the mixing ratio)  
 716 for the three large-scale forcing profiles given in Fig. 1: deep (solid), shallow (long-dashed), and very shallow  
 717 (short-dashed).



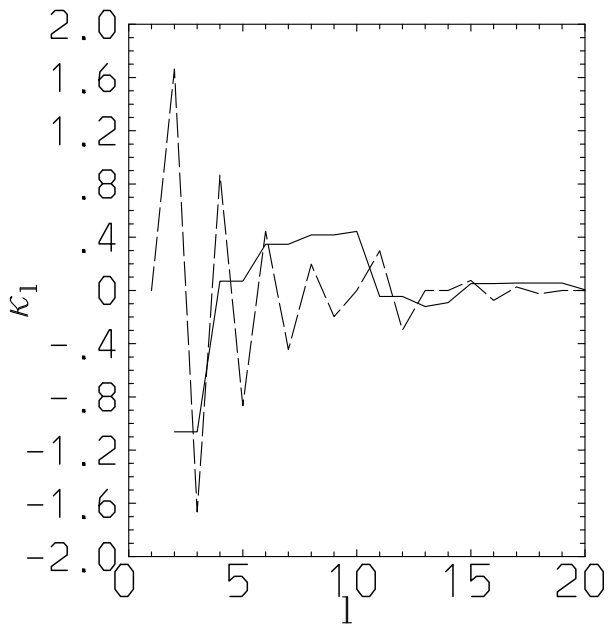
718 FIG. 8. (a) The vertical profiles for the plume spectrum,  $\{\eta_j(z)\}$ , shown as a function of height (horizontal  
719 axis) and the plume index (vertical axis). (b) The plume matrix (*i.e.*, the spectrum of plumes decomposed by the  
720 vertical-velocity normal modes),  $\hat{\eta}_{ij}$ , shown as a function of the normal mode index  $i$  (horizontal axis) and the  
721 plume-type index  $j$  (vertical axis). See Eq. (4.2a) for its definition.



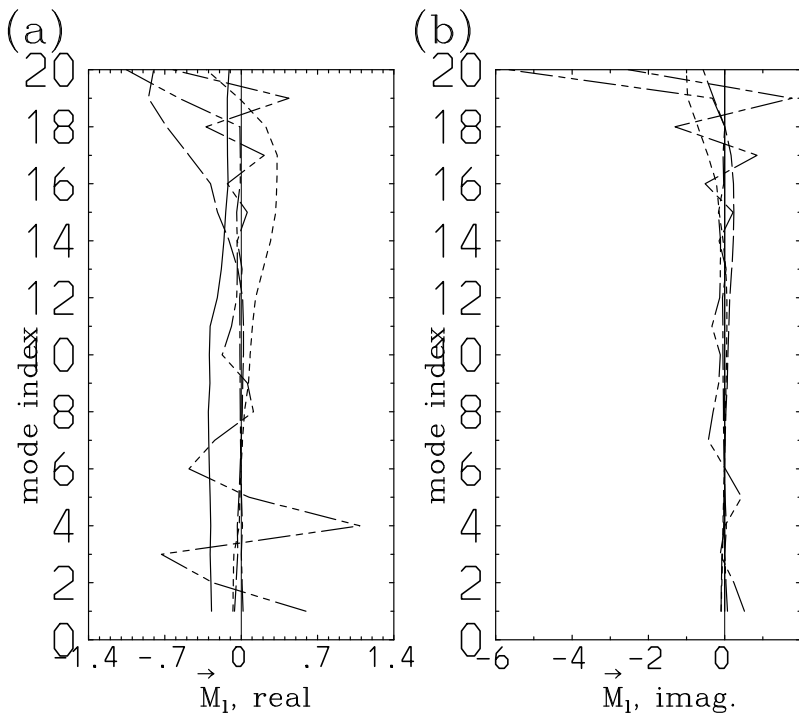
722 FIG. 9. The eigenvalues,  $\lambda_k$ , for the plume matrix,  $\hat{\eta}_{ij}$ , plotted as a function of the index,  $k$ , in decreasing  
 723 order of their absolute value. Both the real (solid) and imaginary (long-dash) parts are shown.



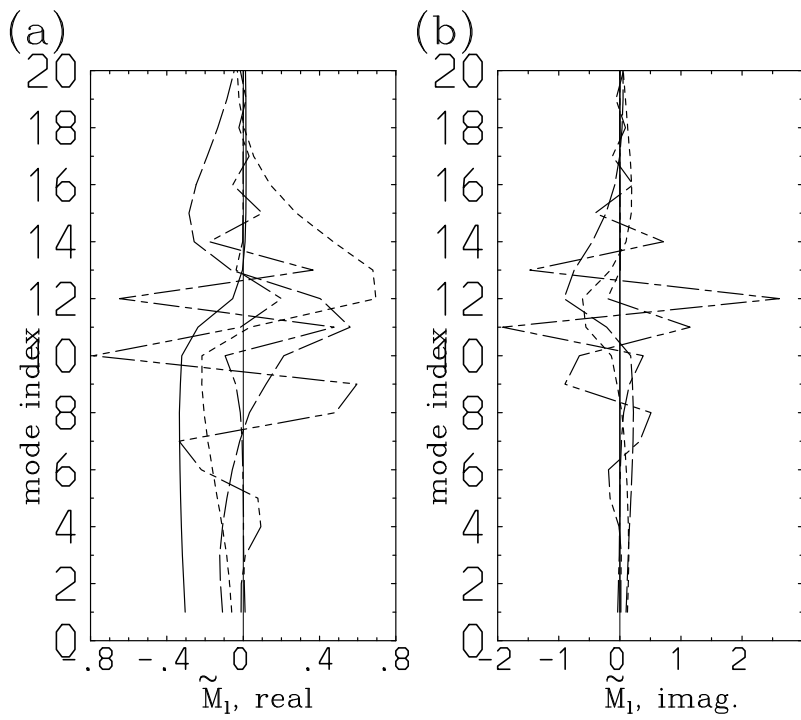
724 FIG. 10. (a) The plume matrix,  $\hat{\eta}_{ij}$ , as in Fig. 8(b), but here following a regularization by retaining only the  
 725 first  $n_c = 16$  modes in Eq. (4.4). (b) The vertical profiles for the plume spectrum,  $\{\eta_j(z)\}$ , as in Fig. 8(a), but  
 726 reconstructed after the matrix regularization as in (a). Although both spectra contain complex values, only the  
 727 real components are shown, the imaginary components being numerically negligible.



728 FIG. 11. The eigenvalues,  $\kappa_l$ , for the interaction matrix,  $\mathbf{K}$ , plotted as a function of the index,  $l$ , in decreasing  
729 order of their absolute value. Both the real (solid) and imaginary (long-dash) parts are shown. An exceptionally  
730 large magnitude for the real component of the first eigenvalue (less than  $-25$ ) is beyond the range of this plot  
731 and is not presented. The 2nd to the 9th eigenvalues constitute a series of complex conjugate pairs, as well as  
732 the 11th and the 12th, and from the 15th to the 18th.



733 FIG. 12. The first eight right-eigenvectors,  $\vec{M}_l$  ( $l = 1, \dots, 8$ ), of the interaction matrix, as defined by Eq. 4.9a.  
 734 (a) Real and (b) imaginary components. The first four vectors are shown by solid, long-dashed, short-dashed,  
 735 and dot-dashed curves. They are followed by four other varying types of the curves. Note that change of scale  
 736 in the horizontal axis.



737 FIG. 13. The first eight left-eigenvectors,  $\tilde{\mathbf{M}}_l$  ( $l = 1, \dots, 8$ ), of the interaction matrix, as defined by Eq. 4.9b.  
 738 Plotted in the same format as for the right-eigenvectors in Fig. 12.